Trifunctional TiO_2 Nanoparticles with Exposed {001} Facets as Additives in Cobalt-Based Porphyrin-Sensitized Solar Cells

Peng Zhai, Tsung-Yu Hsieh, Chen-Yu Yeh, Kamani Sudhir K Reddy, Chi-Chang Hu, Jhih-Hao Su, Tzu-Chien Wei, and Shien-Ping Feng**

In this study, highly mesoporous TiO_2 composite photoanodes composed of functional {001}-faceted TiO_2 nanoparticles (NPs) and commercially available 20 nm TiO_2 NPs are employed in efficient porphyrin-sensitized solar cells together with cobalt polypyridyl-based mediators. Large TiO_2 NPs (approximately 50 nm) with exposed {001} facets are prepared using a fast microwave-assisted hydrothermal (FMAH) method. These unique composite photoanodes favorably mitigate the aggregation of porphyrin on the surface of TiO_2 NPs and strongly facilitate the mass transport of cobalt-polypyridyl-based electrolytes in the mesoporous structure. Linear sweep voltammetry reveals that the transportation of Co(polypyridyl) redox is a diffusion-controlled process, which is highly dependent on the porosity of TiO_2 films. Electrochemical impedance spectroscopy confirms that the FMAH TiO_2 NPs effectively suppress the interfacial charge recombination toward $[Co(bpy)_3]^{3+}$ because of their oxidative {001} facets. In an optimal condition of 40 wt% addition of FMAH TiO_2 NPs in the final formula, the power conversion efficiency of the dye-sensitized cells improves from 8.28% to 9.53% under AM1.5 (1 sun) conditions.

1. Introduction

The fabrication of the first high-efficicency dye-sensitized cells (DSCs) in 1991 resulted in considerable interest because of their low-cost and miniaturized photovoltacis. Innovations over the past two decades have nearly doubled their power conversion efficiency (PCE), and a certified PCE of 13.0% was demonstrated under standard test conditions (AM1.5, 100 mW cm^{-2}).[1] The DSC core contains a sensitizer, which substantially affects the DSC performance along with its compatibility with other DSC components, such as the semiconductor, redox couple, and counter electrode. Among the various highly efficient sensitizers, porphyrins are considered the most promising because of their superior visible light adsorption and molecular design versatility;[2] such superior adsorption enables the use of thin (<5 µm) photoanodes, which facilitate considerably low sensitizer consumption and thus reduce costs, and the design versatility allows functional moieties to be equipped on the heterocyclic body, which enhances optoelectronic properties[3] and obstructs undesirable electron routes.[4]

In contrast to sensitizers, innovations pertaining to DSC redox couples are low because they are merely electron donors and acceptors on the photo electrode and counter electrode sides, respectively, at appropriate redox potentials principally. However, developing effective DSC redox couples requires broader considerations. For the past two decades, I^-/I_3^- was the dominant DSC redox couple because of its excellent electrochemical reversibility, fast dye regeneration, and acceptable recombination at the TiO_2/I_3^- interface. However, I^-/I_3^- corrodes the silver grid lines in large devices and undergoes optical loss in the visible light region and considerable overpotential loss during dye regeneration (high reorganization energy of 0.7 eV). Therefore, novel redox couples, such as $SeCN^-/Se(CN)_3^-$,[5] TEMPO/TEMPO+,[6] $SCN^-/(SCN)_2$,[7] and cobalt polypyridyl complexes,[8] have been proposed as iodine-free alternatives, among which cobalt polypyridyl complexes (Co(polypyridyl)) are of particular interest because of their tunable redox potential and high optical transparency in the visible light region. When a highly efficient porphyrin sensitizer was combined with a Co(polypyridyl) redox couple, a PCE exceeding 12% was successfully demonstrated at a remarkable open-circuit voltage (V_{OC}) exceeding 900 mV.[9]

Despite these advantages, the Co(polypyridyl) system is not perfect: their bulky molecular structure sluggishly transfers between electrodes and their outer-sphere one-electron redox

P. Zhai, Prof. S.-P. Feng
Department of Mechanical Engineering
The University of Hong Kong
Pokfulam Rd., Hong Kong 999077
E-mail: hpfeng@hku.hk
T.-Y. Hsieh, Prof. C.-C. Hu
J.-H. Su, Prof. T.-C. Wei
Department of Chemical Engineering
National Tsing-Hua University
Hsinchu 300, Taiwan
E-mail: tcwei@mx.nthu.edu.tw
Prof. C.-Y. Yeh, K. S. K Reddy
Department of Chemistry
National Chung Hsing University
Taichung 402, Taiwan

DOI: 10.1002/adfm.201501982

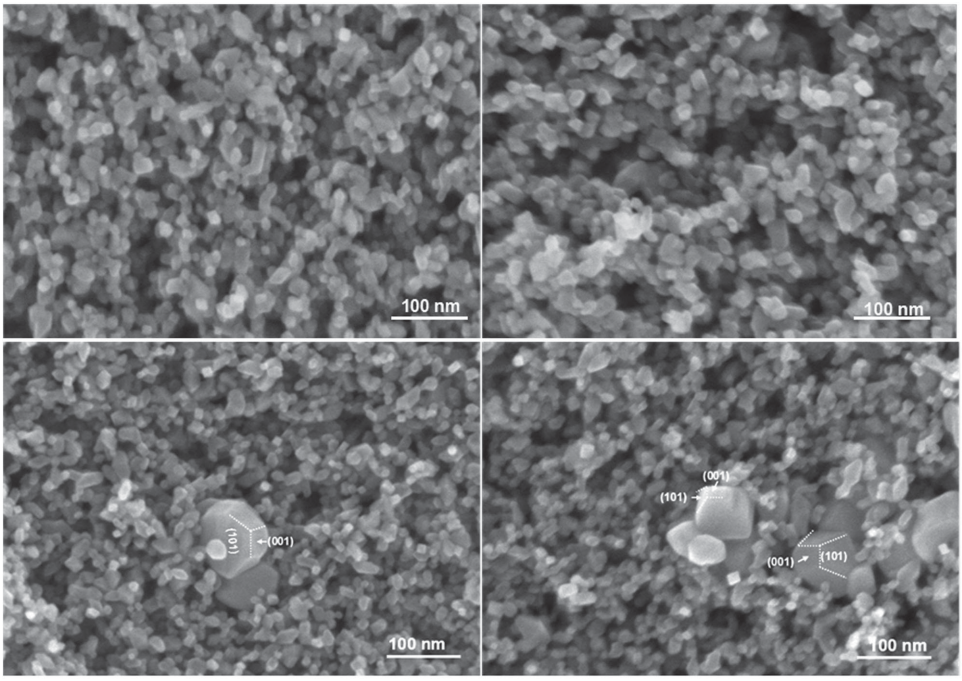

Figure 1. FESEM images of a) commercial 20 nm and b) 30 nm TiO_2 photoanodes, and c) FMAH-20 and d) FMAH-40 TiO_2 photoanodes.

mechanism enables extremely fast electron recombination at the TiO_2/electrolyte interface; the sluggish transfer forces the device to operate under a diffusion-controlled condition, and the fast recombination causes low shunt resistance. Therefore, despite their theoretical superiority, DSCs equipped with porphyrin sensitizers and Co(polypyridyl) redox couples largely fail to outperform those with ruthenium-based sensitizers and the I^-/I_3^- system. Their inferior performance is primarily attributable to the severe molecular aggregation in porphyrin sensitizers induced by π–π stacking of the heterocyclic body on TiO_2 NP surfaces, charge recombination between the electron in the conduction band of the TiO_2 and porphyrin radical cation[10] as well as the sluggish mass transport of cobalt mediators in conventional mesoporous TiO_2 films,[11] which lead to lower short-circuit currents (J_{SC}) and consequently to low PCE.

To overcome the aforementioned drawbacks, several theories have been investigated for actualizing the advantages of cobalt-mediated DSCs. For instance, the TiO_2 particle size was enlarged from 20 nm, common in ruthenium sensitizers, to 30 nm for relieving aggregation.[1] In addition, porphyrin sensitizers with steric hindrance, such as an *ortho* octyloxy phenyl ring on the *meso* position of the porphyrin ring, were molecularly designed to effectively restrain interfacial recombination.[12] Finally, to overcome the drawback of ionic diffusion, Heiniger et al.[13] and Kim and co-workers[14] manipulated the pore sizes and porosities of TiO_2 films by fabricating photoanodes by using large TiO_2 beads. Moreover, Pham et al.[15] fabricated macropores in mesoporous TiO_2 films by using polystyrene templates during TiO_2 filming. These efforts have yielded higher cobalt ion diffusivity compared with conventional TiO_2 films composed of 20 nm NPs.

As discussed, sensitizer aggregation, interfacial recombination, and ionic diffusion are the three technical problems associated with cobalt-mediated porphyrin-sensitized DSCs. In this study, we propose a simple, cost-effective method for simultaneously solving these three technical problems by incorporating homemade TiO_2 NPs (approximately 50 nm) with the exposed {001} facets into commercial 20 nm TiO_2 paste. Adding large TiO_2 NPs reduces the overall surface area of the resultant mesoporous film and therefore alleviates porphyrin aggregation; moreover, the pore volume and average pore size in the mesoporous film increase substantially, consequently facilitating Co(polypyridyl) ion diffusion. Principally, the high-energy {001}-faceted TiO_2 NPs effectively suppress interfacial recombination, thus further enhancing the photovoltaic performance. Finally, the PCE of Co(polypyridyl)-based YD2-oC8-sensitized cells are improved from 8.28% to 9.53% under AM1.5 and 100 mW cm^{-2} illumination.

2. Results and Discussion

2.1. Characterization of {001}-Faceted TiO_2 Nanoparticles

Figure 1a,b illustrates the field emission scanning electron microscope (FESEM) images of TiO_2 mesoporous films fabricated using commercial 20 nm (Ti-2105, 99.9% anatase TiO_2, Eternal, Taiwan) and 30 nm (30NR-D, Dyesol, Australia) TiO_2 pastes, respectively; both images reveal typical mesoporous structures but with different particle sizes. The film fabricated using the 30 nm TiO_2 paste (Figure 1b) has larger particles and wider pores compared with that fabricated using 20 nm TiO_2 paste (Figure 1a). The wider pore structure provides spacious channels for bulky Co(polypyridyl) ion transfer between the mesoporous structure and the bulk electrolyte, thus preventing the device from operating under the mass transfer limiting

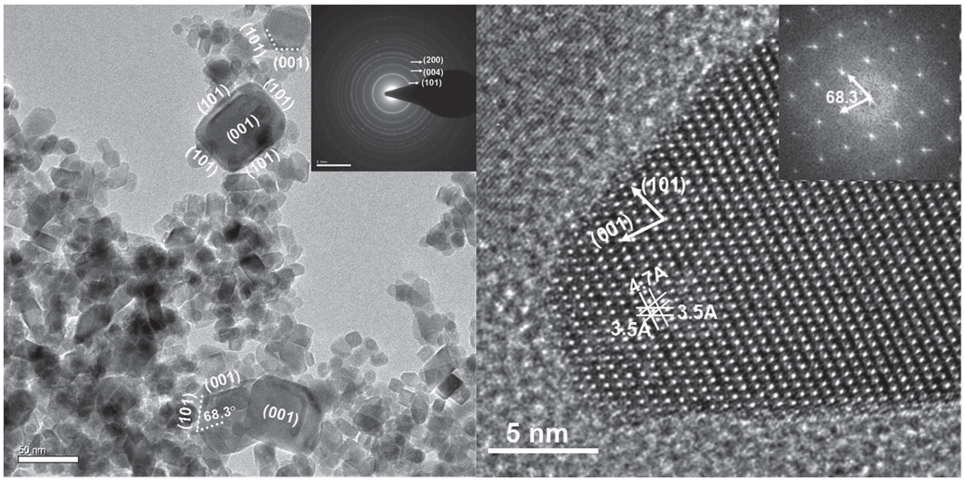

Figure 2. a) TEM images of FMAH-40 TiO_2 NPs; dotted lines indicate the (001) and (101) facets of FMAH TiO_2 NPs; inset indicates the corresponding SAED pattern. b) HRTEM image of a hexagonal FMAH TiO_2 NP shape; inset shows the FFT pattern indexed as the [010] zone axis.

condition. The 50 nm TiO_2 NPs with exposed {001} facets were synthesized using a fast microwave-assisted hydrothermal (FMAH) method and a commercial instrument. FMAH 50 nm TiO_2 was incorporated into commercial 20 nm TiO_2 paste by adding FMAH 50 nm TiO_2 at 40% and 20% (wt% with respect to commercial 20 nm TiO_2 NPs) immediately after hydrothermal growth (hereafter denoted as FMAH-40 and FMAH-20 TiO_2 NPs, respectively). Experimentally, FMAH 50 nm TiO_2: commercial 20 nm TiO_2 ratio exceeding 40% fails to produce a film with adequate mechanical strength. The FMAH-20 and FMAH-40 TiO_2 films are shown in Figure 1c,d, respectively. In both images, the larger FMAH TiO_2 NPs with truncated octahedron morphologies of clear {001} and {101} facets are dispersed in 20 nm NPs, and the commercial 20 nm NPs are irregularly shaped. Furthermore, the structure has numerous voids in the vicinity of the FMAH TiO_2 particles, indicating that FMAH TiO_2 creates additional channels. **Figure 2**a depicts a transmission electron microscope (TEM) image of the FMAH-40 TiO_2 NPs. The FMAH TiO_2 NPs demonstrate distinctive profiles when viewed from various directions: hexagons (lateral view) and squares (top view) of truncated octahedra (bipyramid structure). The difference in contrast between the central and peripheral sections of the TiO_2 NPs is attributable to the blunt edges of the {101}-faceted NPs.[16] The interfacial angle between the top two parallel and lateral surfaces are approximately 68.3°, identical to the theoretical interfacial angle between the {101} and {001} facets in anatase crystals. The selected-area electron diffraction (SAED) pattern (inset) suggests that FMAH TiO_2 NPs have well-defined diffraction rings in the anatase phase. The high-resolution TEM (HRTEM) image (Figure 2b) shows the crystal orientation of {101} and {001} facets with an interfacial angle of 68.3°. The lattice spacing of 3.5 and 4.7 Å correspond to the {101} and {002} planes, respectively, indicating that the top and bottom surfaces exposed by truncation are bound by a {001} facet. Furthermore, the fast Fourier transform (FFT) image (inset) is indexed as the [010] zone axis diffraction, and the diffraction spots are assigned to the {001} and {101} facets.[17] For comparison, TEM images of 20 and 30 nm TiO_2 NPs are provided in Figure S1, Supporting Information; both images exhibit identical irregular morphologies but with dissimilar particle sizes.

X-ray powder diffraction (XRD) was conducted to validate the crystalline structure of the samples. In **Figure 3**a, the XRD pattern exhibits strong diffraction peaks at 25°, 38°, and 48°, which are characteristic (101), (004), and (200) planes of anatase TiO_2.[18] All diffraction peaks of the 30 nm, FMAH-20, and FMAH-40 TiO_2 films were more intense than those of the conventional 20 nm TiO_2 film, revealing that a larger NP size yields enhanced crystallinity. The FMAH-40 TiO_2 NPs exhibits the strongest (004) and (200) diffraction peaks; the relative ratio of the (004) peak diffraction intensity to that of the (101) peak of FMAH-40 and FMAH-20 is approximately 30.6% and 20.0%, respectively, whereas that of the 30 nm film was lower (18.5%), which strongly implies that the oriented growth is along the (001) direction in FMAH TiO_2 NPs.[19] Figure 3b illustrates plots of the nitrogen adsorption and desorption isotherms of these TiO_2 NPs, and Figure 3c shows their pore-size distribution obtained using the Barrett–Joyner–Halenda (BJH) model. The pronounced hysteresis loop in Figure 3b is a type IV isotherm typical for mesoporous materials. The four isotherms are similar; FMAH-40 TiO_2 yielded lower adsorption volumes, indicating that the high-ratio blending of the 50 nm TiO_2 NPs does not change its essential microstructural characteristics but reduces only the surface area available for the N_2 adsorption. **Table 1** shows comprehensive particle characteristics, including specific surface area (S_{BET}), pore volume (V_{BJH}), and average pore size. These results reveal that the FMAH-40 TiO_2 NPs demonstrate the highest V_{BJH} and lowest S_{BET}, whereas commercial 20 nm TiO_2 NPs, which are widely used in iodine-based ruthenium-sensitized cells, have the lowest V_{BJH} (0.459 $cm^3\ g^{-1}$) and highest S_{BET} (85.135 $m^2\ g^{-1}$). S_{BET} is usually associated with sensitizer loading, and V_{BJH} with the space that can be occupied by the electrolyte. Table 1 shows that the 30 nm TiO_2 NPs meliorate the problems associated with 20 nm TiO_2 NPs by reducing the S_{BET} (to nearly 75.104 $m^2\ g^{-1}$), which alleviates porphyrin sensitizer aggregation, and by increasing V_{BJH} (to nearly 0.531 $cm^3\ g^{-1}$), which creates approximately 15.7% more space for electrolyte accommodation; moreover,

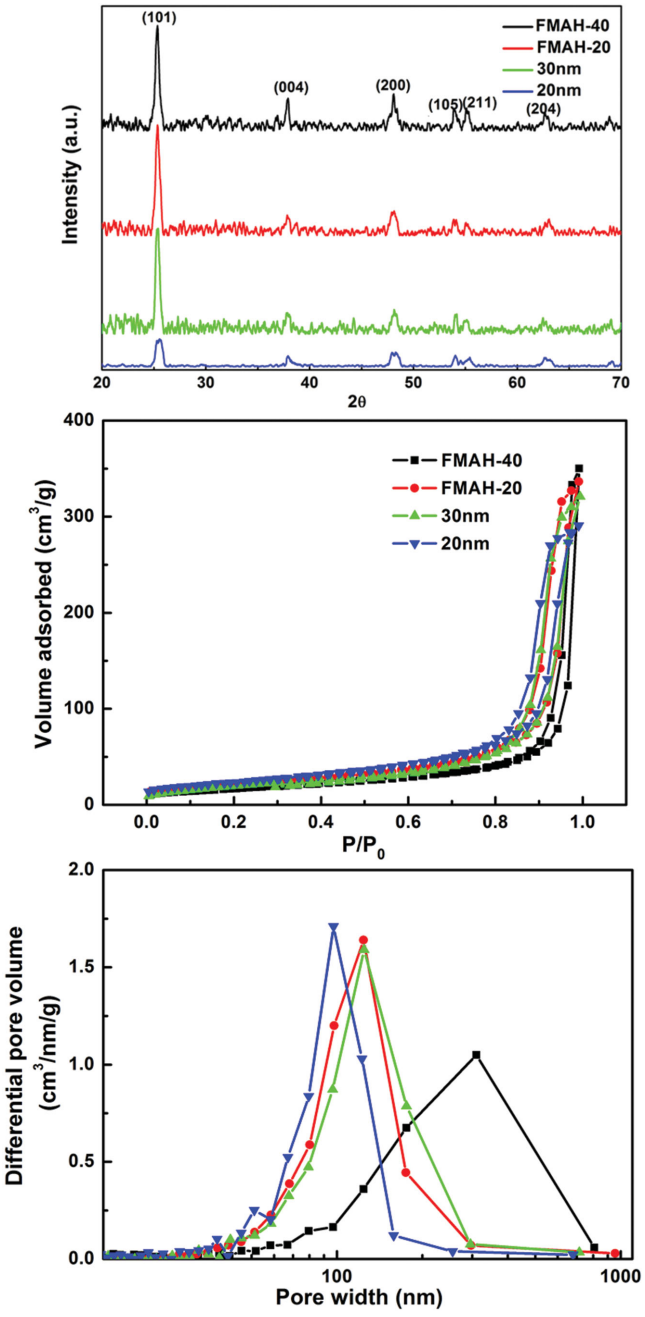

Figure 3. a) XRD spectra, b) N_2 adsorption–desorption isotherms, and c) pore size distributions.

Table 1. Specific surface areas, pore volumes, average pore sizes, and dye-loading of the 20 nm, 30 nm, FMAH-20, and FMAH-40 TiO_2 NPs.

Sample	Specific surface area [m^2 g^{-1}]	Pore volumes [cm^3 g^{-1}]	Average pore size [nm]	Dye loading $\times 10^{-5}$ [mol cm^{-2} μm^{-1}]
FMAH-40	61.689	0.539	175.604	1.244
FMAH-20	78.264	0.515	124.074	1.278
30 nm	75.104	0.531	124.659	1.227
20 nm	85.135	0.459	97.189	1.955

the average pore size expands by nearly 28.3% (from 97.189 to 124.659 nm), which is essential for bulky cobalt redox ions. To the best of our knowledge, this is the first quantitative report on the superiority of 30 nm TiO_2 NPs in a cobalt redox system. S_{BET} and V_{BJH} change when the widely used 20 nm NPs are blended with FMAH 50 nm TiO_2 NPs. The measured S_{BET} and V_{BJH} of FMAH-20 TiO_2 are consistent with those of commercial 30 nm NPs. Remarkably, when the blending ratio of the FMAH TiO_2 NPs reaches 40 wt%, the measured S_{BET} and V_{BJH} are 61.689 m^2 g^{-1} and 0.539 cm^3 g^{-1}, respectively, and the largest pore size (i.e., 175.604 nm) is obtained. These three values, which substantially deviate from those of 20 nm NPs, are beneficial the cobalt-based porphyrin-sensitized system. Photographs of the YD2-oC8-sensitized TiO_2 films are shown in the upper panel of Figure S2, Supporting Information. At the same immersion time, the 20 nm TiO_2 NPs exhibit a dark shade of green, whereas the other three films exhibit lighter and visually indistinguishable shades. Sensitizer loading of these films was measured using ultraviolet–visible (UV–vis) spectroscopy after desorbing the sensitizer by using a published technique,[13] and it is reported in the right-most column of Table 1. Assuming that the kinetics of chemisorption of YD2-oC8 on TiO_2 surfaces is independent of particle size, 20 nm NPs adsorbed nearly 60% more YD2-oC8 than did the other three samples. Because the S_{BET} difference between the 20 nm and FMAH-40 TiO_2 NPs is nearly 38%, we conclude that a considerable amount of YD2-oC8 is collectively adsorbed on 20 nm NPs. This intermolecular aggregation phenomenon is digressively discussed in the Supporting Information.

2.2. Electrochemical Characterization and DSC Performance

Figure 4a illustrates the *I–V* curves of YD2-oC8-sensitized cells with a Co(polypyridyl) electrolyte under AM1.5 100 mW cm^{-2} illumination, and **Table 2** shows a summary of the corresponding *I–V* parameters. The photoanode composed solely of 20 nm TiO_2 NPs delivers a J_{SC} of 12.56 mA cm^{-2}, V_{OC} of 0.87 V, fill factor (FF) of 0.75, and PCE of 8.28%. For the photoanode comprising 30 nm TiO_2 NPs, J_{SC} increases remarkably to 14.90 mA cm^{-2}, whereas V_{OC} and FF decrease to 0.86 V and 0.69, respectively; here, the PCE is enhanced to 8.92%. As stated earlier, the 20 nm TiO_2 photoanode adsorbs nearly 60% more YD2-oC8 than the 30 nm TiO_2 photoanode does, but its J_{SC} is inexplicably lower by nearly 20%. For a 3 μm sensitized photoanode, the J_{SC} is positively correlated with the sensitizer quantity because light harvesting is usually unsaturated. Therefore, the result suggests that the inferior mass transport capability of 20 nm TiO_2 photoanode dominates the PCE. The FMAH-40 TiO_2 photoanode yields the highest J_{SC} and V_{OC} among all samples (15.41 and 0.89 V, respectively), and an FF and PCE of 0.70 and 9.53%, respectively.

To confirm that J_{SC} is predominantly controlled by the mass transfer of Co(polypyridyl), we investigated the electrolyte diffusion within the TiO_2 films by using linear sweep voltammetry (LSV). Here, we designed a modified thin, two-electrode cell, as shown in the inset of Figure 4b. Two fluorine-doped tin oxide (FTO) electrodes were coated with PVP-capped platinum nanocluster (PVP-nPt) NPs[20]; one of them was screen

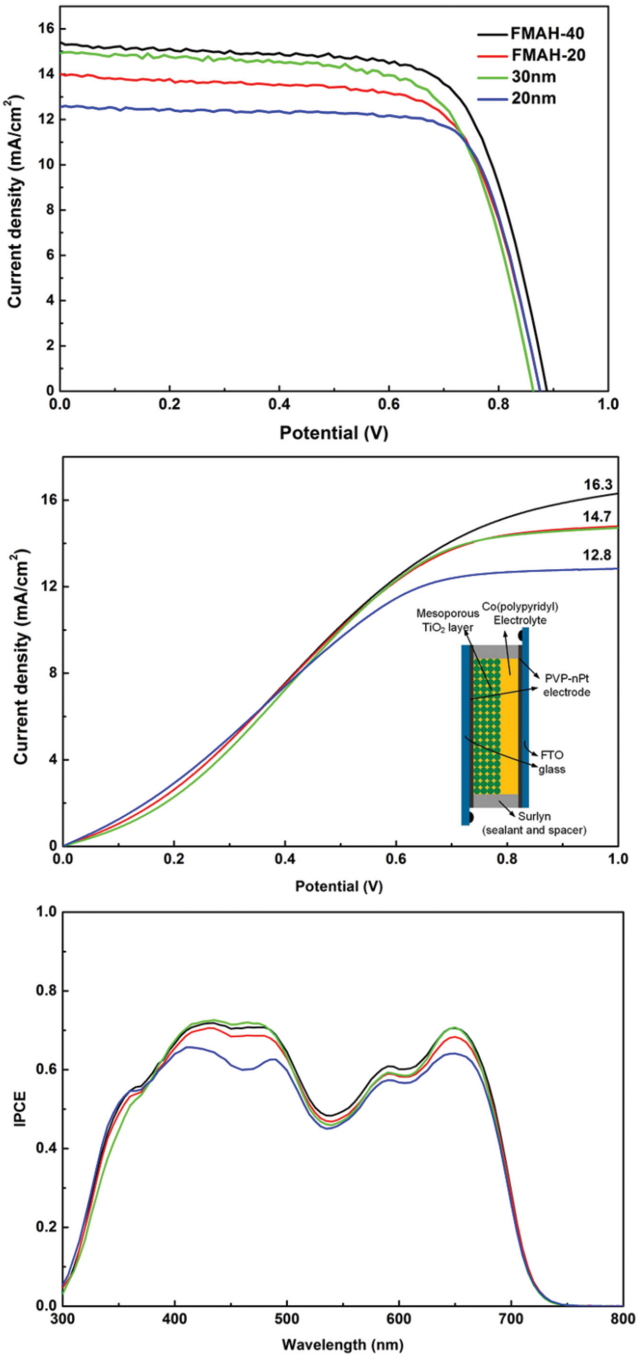

Figure 4. a) Current density–voltage characteristic of DSCs under 1 sun illumination. b) LSV measurement with the cells undergoing potential from 0 to 1 V at a scan rate of 10 mV s^{-1}; inset indicates a schema of the modified thin, two-electrode cell; c) IPCE spectra.

printed with a 3 µm thick TiO_2 film and laminated with a PVP-nPt-coated FTO film through hot-pressing with a Surlyn spacer. Finally, the Co(polypyridyl) electrolyte was injected into the gap between the two electrodes. Figure 4b shows the LSV of various nonsensitized mesoporous TiO_2 films in the dark and under forward bias from 0 to 1 V at a scan rate of 10 mV s^{-1}. The current increases with the scanning potential

Table 2. Photovoltaic characteristics of DSCs obtained using different photoanodes under AM1.5 100 mW cm^{-2} illumination.

Sample	J_{SC} [mA cm^2]	V_{OC} [V]	FF	PCE [%]
FHAM-40	15.41	0.89	0.70	9.53
FHAM-20	14.02	0.88	0.70	8.57
30 nm	14.90	0.86	0.69	8.92
20 nm	12.56	0.88	0.75	8.28

until plateauing, indicating the transition from kinetic control to mass transfer control. The current recorded in the plateau region is the limiting current (J_{lim}) and is used as an index of mass transport capability of this electrochemical systems. The J_{lim} of the 20 nm NP film is 12.8 mA cm^{-2}, which matches the J_{SC} of its device, evidencing that the device operates under the mass transfer limiting condition. In the 30 nm NPs, the J_{lim} value increases to 14.7 mA cm^{-2} because of the improved V_{BJH}. In our experiment, the ratio of V_{BJH} and J_{lim} for both the 30 and 20 nm NPs is 1.16, suggesting a linear relationship between the pore volume of a mesoporous film and its mass transfer capability. The J_{SC} of the 30 nm TiO_2 device is 14.9 mA cm^{-2}, which is also attributable to the mass transport limitation. As discussed in the preceding section, V_{BJH} increases considerably after the addition of FMAH TiO_2 NPs; the J_{lim} of the FMAH-20 and FMAH-40 photoanodes are improved to 14.6 and 16.3 mA cm^{-2}, respectively. The J_{SC} of the FMAH-40 photoanode device is 15.7 mA cm^{-2}, indicating that the supply of Co(polypyridyl) is adequate and that the cell is no longer under diffusion control. The superiority in mass transport capability of FMAH-40 photoanode over 20 nm TiO_2 photoanode is further checked by measuring the short circuit current dynamics of the device made from FMAH-40 and 20 nm TiO_2 photoanode. Shown in Figure S4a, Supporting Information, because of mass transport limitation has not reached yet, the J_{SC} of YD2-oC8 sensitized photoanode made from FMAH-40 TiO_2 remains constant during the light pulse over 3 s under 1 sun illumination, while the J_{SC} of photoanode composed of solely 20 nm NPs exhibits obvious diffusive decay, echoing the improvement on mass transport capability of FMAH NPs. The current decay is alleviated when the light intensity becomes 0.1 sun (Figure S4b, Supporting Information). Figure 4c illustrates the incident photon-to-current conversion efficiency (IPCE) spectra of the devices with various photoanodes as a function of wavelengths ranging from 300 to 800 nm. Introducing the FMAH TiO_2 NPs considerably enhances the quantum efficiency of the photoanodes over the entire spectral range compared with that of the photoanode with 20 nm NPs, confirming that the improvement on J_{SC} by FMAH-TiO_2-NP incorporation does not stem from the improvement of optical properties, such as the scattering effect. The IPCE is quite consistent with their J_{SC}, confirming that porphyrin aggregation and cobalt ion diffusivity are mitigated by the enlarged porosity of the TiO_2 photoanode.[21]

We investigated the electronic properties of DSCs with various photoanodes by using electrochemical impedance spectroscopy in the frequency range 100 kHz–0.1 Hz at various forward bias potentials under dark conditions. The recorded

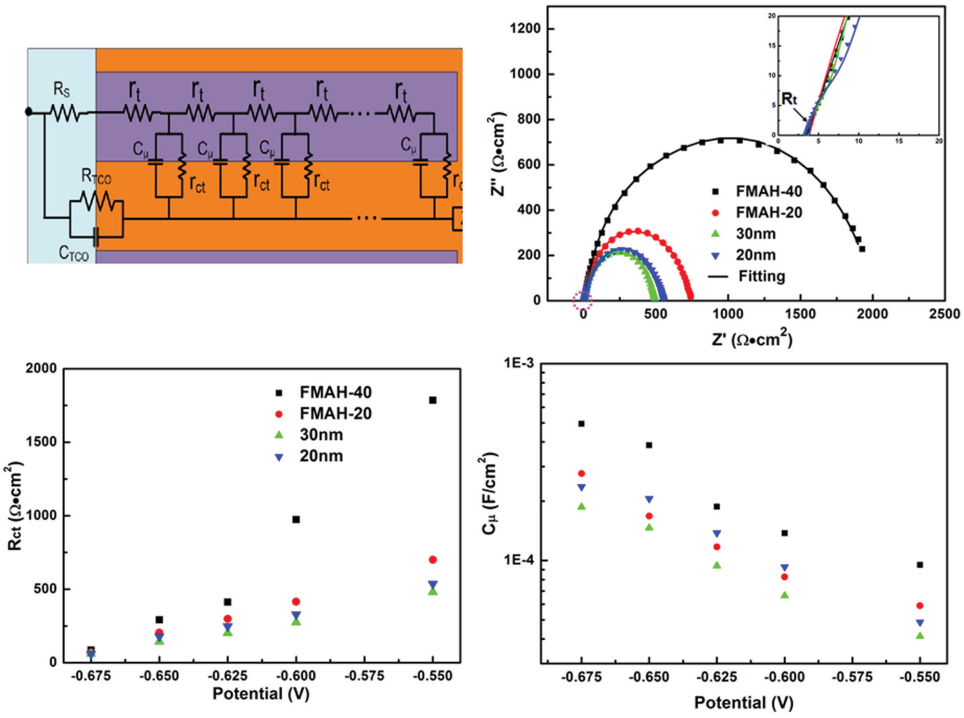

Figure 5. a) TLM of a DSC; b) Nyquist plot of the DSCs at an applied potential of –0.55 V under dark condition; inset: magnified image of the red circle, which clearly shows the charge transport resistance (R_t); c) Charge transfer resistance (R_{ct}) and d) capacitance (C_μ) with respect to the applied intermediate bias potentials under the dark condition.

spectra were fitted using the transmission line model (TLM)[22] (**Figure 5**a) and Zview software (Scribner, UK). As the forward bias increased, the photoanode gradually became electronically conductive, and the parameters determining the electronic properties of a photoanode such as chemical capacitance (C_μ), charge transport resistance (R_t) in the TiO_2 film, and charge transfer resistance (R_{ct}) at the TiO_2/sensitizer/electrolyte interface were extracted. Figure 5b depicts the Nyquist plot of the experimental data (solid circles) and the fitting curve (solid lines) recorded at a forward bias of 0.55 V. The widest variation occurs in the diameter of the arcs in the middle frequency region, which represents R_{ct}. In the FMAH-40 photoanode, R_{ct} at this bias is nearly four times that of conventional 20 nm NPs, suggesting a slower recombination reaction at the TiO_2/sensitizer/electrolyte interface, which is beneficial for charge collection. Figure 5c,d presents R_{ct} and C_μ as a function of the applied bias. Clearly, FMAH TiO_2 NPs restrain interfacial recombination. As affirmed by the aforementioned FESEM, TEM, and XRD analyses, the FMAH TiO_2 NPs possess exposed {001} facets; the high energy {001} facets (0.90 J m^{-2}) are oxidative sites and are thus less likely to function as photoelectron reduction sites.[23] In comparison, the photoanodes comprising the 20 and 30 nm TiO_2 NPs fail to suppress interfacial recombination because of their nonspecific orientation. Therefore, we used the FMAH TiO_2 NPs as recombination inhibitors in mesoporous TiO_2 films composed of 20 nm TiO_2 NPs, which also simultaneously satisfies the light adsorption criteria. This charge recombination inhibition is further explained by the C_μ variation shown in Figure 5d. In principle, C_μ represents the filling of trap states below the TiO_2 conduction band (CB). As noted, the C_μ of the FMAH-40 photoanode is approximately a half order of magnitude greater than that of the 20 nm photoanode because of the more spacious mesoporous structure and exposed {001} facets of the FMAH-40 photoanode, which adequately accommodates Co(polypyridyl). By contrast, the 20 nm photoanode renders a higher density of states.[24] Remarkably, the crystallinity of the 30 nm NPs increases with the NP size, which is affirmed by the profound diffraction peaks relative to those of the 20 nm NPs in the XRD pattern. However, lacking in exposed {001} facets, the 30 nm TiO_2 photoanode is marred by low R_{ct} and C_μ because its spacious mesoporous structure enables the bulky cobalt mediator to access several TiO_2 recombination centers. Table 2 and Figure 4a indicate that among all devices, the DSC composed of the FMAH-40 photoanode yields the highest V_{OC} (0.89 V); because its J_{SC} value increases from 12.56 to 15.41 mA cm^{-2}, the V_{OC} is lower than that for the 20 nm TiO_2 photoanode as more photoelectrons are recaptured by the oxidized Co(polypyridyl) ions. A reasonable estimation for this effect is the measured V_{OC} of 0.86 V for the 30 nm TiO_2 photoanode, which delivers a J_{SC} value similar to that of the FMAH-40 (14.90 mA cm^{-2}). The current study reveals that the addition of exposed {001}-faceted FMAH TiO_2 NPs to 20 nm NPs maintains a high V_{OC} because of recombination inhibition.

3. Conclusion

We developed a simple approach for fabricating a cost-efficient TiO_2 photoanode for YD2-oC8 DSCs using a Co(polypyridyl) mediator. Adding FMAH TiO_2 NPs to commercial 20 nm TiO_2

NPs affords several benefits, such as low specific surface area and high pore volume, which alleviate porphyrin aggregation and facilitate the mass transport of the mediator. Principally, the highly reactive {001}-faceted FMAH TiO_2 NPs suppress interfacial recombination, which further improve photovoltaic performance. DSCs equipped with cobalt-based electrolytes usually encounter the mass transport problem in mesoporous TiO_2 films, whereas porphyrin-sensitized DSCs exhibit poor device reproducibility because of intermolecular aggregation. The composite TiO_2 film fabricated in the current study simultaneously overcomes these technical problems without the necessity of a complicated synthesis procedure and precise NP growth control. The synthesis of FMAH TiO_2 NPs and the procedures involved in creating their films are scalable, reproducible, and feasible and can serve as the standard for future manufacturing and assessment of cobalt-based porphyrin-sensitized DSCs.

4. Experimental Section

Preparation of FMAH TiO_2 NPs: The phase-pure, nanocrystalline anatase TiO_2 was prepared by a fast FMAH method. All chemicals were analytical grade and used without further purification. The detail of preparation 50 nm FMAH nanoparticle is as follows: 5 mL $TiCl_3$ was oxidized by stoichiometric H_2O_2 to Ti^{4+}. Then, 20 mL of 0.5 M H_2SO_4 was added into the solution, followed by high-intensity sonication for 25 min. The mixture was then transferred to a microwave reactor (CEM, USA) to form TiO_2 NPs at 200 °C for 20 min. The resultant solution was cooled down to room temperature, centrifuged and rinsed with deionized (DI) water sequentially. The final precipitates were dried in an oven at 85 °C for 12 h to obtain the white pristine TiO_2 NPs. The anatase FMAH TiO_2 NPs were obtained after annealing at 700 °C for 2 h in air.

Preparation of TiO_2 Paste: First, the addition of FMAH TiO_2 into commercial 20 nm TiO_2 was done by mixing FMAH TiO_2 "dry" powder with "wet" 20 nm TiO_2 powder. To do this, we ordered 20 nm TiO_2 wet powder (dry powder dispersing in ethanol) from Eternal Chemicals, a company supplies 20 nm TiO_2 paste for DSC in Taiwan. With the solid content information provided by provided by Eternal Chemicals, the stoichiometry of FMAH addition becomes easy. Therefore, the "wt%" is defined as the ratio of dry FMAH powder with respect to total dry TiO_2 powder (FMAH + 20 nm). Experimentally, the addition of dry FMAH TiO_2 into wet 20 nm TiO_2 is followed by redispersing in excess ethanol under sonication. This TiO_2 colloidal is made to screen-printable paste by a published process described elsewhere.[25] The final composition in the paste 18:5:77 for TiO_2:ethyl cellulose (30–50 mPa, Fluka) and terpineol (98%, Fluka).

Fabrication of TiO_2 Photoanodes, DSC Assembly: Mesoporous TiO_2 films composed of commercial 20 nm (Ti-2105), 30 nm (30NR-D, Dyesol, Australia), FMAH-20, and FMAH-40 TiO_2 NP slurries were screen-printed on FTO glass. The thicknesses of all films were controlled to 3 μm, and a 3 μm scattering layer (JGC C&C PST400) was subsequently screen-printed on the mesoporous films. The sensitizer, YD2-oC8, was impregnated by immersing the aforementioned bilayer TiO_2 films into a tetrahydrofuran/ethanol (1:1) solution containing 0.2×10^{-3} M YD2-oC8 for 2 h. To prevent YD2-oC8 aggregation, chenodeoxycholic acid (CDCA, 0.4×10^{-3} M) was added to the YD2-oC8 solution as the coadsorbent. The FTO surface and the bilayer TiO_2 film were modified through typical $TiCl_4$ pre- and post-treatment, respectively.[26]

PVP-nPt was used as the counter electrode; the details of PVP-nPt technology are described in a previous study.[20] DSCs were assembled by sandwiching the YD2-oC8 sensitized photoanode and the PVP-nPt counterelectrode with a hot-melt film (Surlyn, 30 μm thick, Dupont, USA) serving as the spacer. An appropriate amount of liquid electrolyte (45×10^{-3} M $Co(bpy)_3(TFSI)_3$ [where $Co(bpy)_3(TFSI)_3$ = tris(2,2′-bipyridine)cobalt(III)bis-(trifluoromethanesulfonimide)], 165×10^{-3} M $Co(bpy)_3(TFSI)_2$, 100×10^{-3} M lithium bis(trifluoromethane sulfonyl) imide (LiTFSI), and 400×10^{-3} M tri-*n*-butyl phosphate (TBP) in acetonitrile (AN)) was injected into the gap between the two electrodes through a small hole predrilled on the counter electrode. Finally, the injection hole was sealed using a thin cover glass and UV-curable glue.

Characterization and Measurement: The topography of the 20 nm, 30 nm, FMAH-20, and FMAH-40 TiO_2 photoanodes were investigated using FESEM (S-4800, Hitachi, Japan). TEM (ARM200F, JEOL, Japan) and HRTEM were employed to observe the TiO_2 NPs. The crystallographic structure of the samples was recorded using an XRD (Siemens D500) operated at 40 kV and 30 mA. A NOVA 1200e surface area and pore size analyzer (Quantachrome Instruments, USA) was employed to examine the specific surface area and average pore size of the samples by using nitrogen (N_2) adsorption–desorption isotherms at 77 K. Furthermore, UV–vis spectra were recorded using a HP8453 spectrophotometer. A photomask (6 × 6 mm) controlled the area of light exposure in the subsequent *I–V* scan, which was recorded using a computer-controlled digital source meter (Keithley 2400) under simulated solar irradiation (AM1.5, 100 mW cm^{-2}, PEC-L15, PECCELL Technologies, Japan). The IPCE was measured as a function of wavelength, ranging from 300 to 800 nm, using PEC-S20 (PECCELL Technologies, Japan). The EIS spectra were measured by scanning the DSCs with a potentiostat from 100 kHz to 0.1 Hz at 5 mV amplitude and various forward biases under dark conditions (1286 Solartron and 1255 Solartron, UK).

Supporting Information

Supporting Information is available from the Wiley Online Library or from the author.

Acknowledgements

This work was supported by the General Research Fund of the Research Grants Council of Hong Kong Special Administrative Region (Award No. HKU 712213E). In addition, financial support from Chang Chun Petro Chemicals Co. Ltd., Chang Chun Plastics Co. Ltd., and Ministry of Science and Technology of ROC (Taiwan) under Contract No. 103–2622-E-007–025 and 103–2221-E-007–121-MY2 are acknowledged.

Received: May 13, 2015
Revised: July 14, 2015
Published online: September 9, 2015

[1] a) S. Mathew, A. Yella, P. Gao, R. Humphry-Baker, B. F. Curchod, N. Ashari-Astani, I. Tavernelli, U. Rothlisberger, M. K. Nazeeruddin, M. Grätzel, *Nat. Chem.* **2014**, *6*, 242; b) C.-Y. Chen, M. Wang, J.-Y. Li, N. Pootrakulchote, L. Alibabaei, C.-H. Ngoc-le, J.-D. Decoppet, J.-H. Tsai, C. Grätzel, C.-G. Wu, *ACS Nano* **2009**, *3*, 3103.

[2] a) L.-L. Li, E. W.-G. Diau, *Chem. Soc. Rev.* **2013**, *42*, 291; b) H. Imahori, T. Umeyama, S. Ito, *Acc. Chem. Res.* **2009**, *42*, 1809; c) T. Higashino, H. Imahori, *Dalton Trans.* **2015**, *44*, 448; d) K. Kurotobi, Y. Toude, K. Kawamoto, Y. Fujimori, S. Ito, P. Chabera, V. Sundström, H. Imahori, *Chem. Eur. J.* **2013**, *19*, 17075; e) J. Luo, M. Xu, R. Li, K.-W. Huang, C. Jiang, Q. Qi, W. Zeng, J. Zhang, C. Chi, P. Wang, *J. Am. Chem. Soc.* **2013**, *136*, 265.

[3] a) C.-L. Wang, Y.-C. Chang, C.-M. Lan, C.-F. Lo, E. W.-G. Diau, C.-Y. Lin, *Energy Environ. Sci.* **2011**, *4*, 1788; b) C.-P. Hsieh, H.-P. Lu, C.-L. Chiu, C.-W. Lee, S.-H. Chuang, C.-L. Mai, W.-N. Yen, S.-J. Hsu, E. W.-G. Diau, C.-Y. Yeh, *J. Mater. Chem.* **2010**, *20*, 1127.

[4] Y.-C. Chang, C.-L. Wang, T.-Y. Pan, S.-H. Hong, C.-M. Lan, H.-H. Kuo, C.-F. Lo, H.-Y. Hsu, C.-Y. Lin, E. W.-G. Diau, *Chem. Commun.* **2011**, *47*, 8910.

[5] P. Wang, S. M. Zakeeruddin, J. E. Moser, R. Humphry-Baker, M. Grätzel, *J. Am. Chem. Soc.* **2004**, *126*, 7164.
[6] Z. Zhang, P. Chen, T. N. Murakami, S. M. Zakeeruddin, M. Grätzel, *Adv. Funct. Mater.* **2008**, *18*, 341.
[7] G. Oskam, B. V. Bergeron, G. J. Meyer, P. C. Searson, *J. Phys. Chem. B* **2001**, *105*, 6867.
[8] a) J.-H. Yum, E. Baranoff, F. Kessler, T. Moehl, S. Ahmad, T. Bessho, A. Marchioro, E. Ghadiri, J.-E. Moser, C. Yi, *Nat. Commun.* **2012**, *3*, 631; b) S. M. Feldt, E. A. Gibson, E. Gabrielsson, L. Sun, G. Boschloo, A. Hagfeldt, *J. Am. Chem. Soc.* **2010**, *132*, 16714; c) S. A. Sapp, C. M. Elliott, C. Contado, S. Caramori, C. A. Bignozzi, *J. Am. Chem. Soc.* **2002**, *124*, 11215; d) M. J. DeVries, M. J. Pellin, J. T. Hupp, *Langmuir* **2010**, *26*, 9082; e) B. M. Klahr, T. W. Hamann, *J. Phys. Chem. C* **2009**, *113*, 14040.
[9] A. Yella, H.-W. Lee, H. N. Tsao, C. Yi, A. K. Chandiran, M. K. Nazeeruddin, E. W.-G. Diau, C.-Y. Yeh, S. M. Zakeeruddin, M. Grätzel, *Science* **2011**, *334*, 629.
[10] a) H. Imahori, S. Kang, H. Hayashi, M. Haruta, H. Kurata, S. Isoda, S. E. Canton, Y. Infahsaeng, A. Kathiravan, T. r. Pascher, *J. Phys. Chem. A* **2010**, *115*, 3679; b) S. Ye, A. Kathiravan, H. Hayashi, Y. Tong, Y. Infahsaeng, P. Chabera, T. r. Pascher, A. P. Yartsev, S. Isoda, H. Imahori, *J. Phys. Chem. C* **2013**, *117*, 6066.
[11] J. J. Nelson, T. J. Amick, C. M. Elliott, *J. Phys. Chem. C* **2008**, *112*, 18255.
[12] C.-L. Wang, C.-M. Lan, S.-H. Hong, Y.-F. Wang, T.-Y. Pan, C.-W. Chang, H.-H. Kuo, M.-Y. Kuo, E. W.-G. Diau, C.-Y. Lin, *Energy Environ. Sci.* **2012**, *5*, 6933.
[13] L. P. Heiniger, F. Giordano, T. Moehl, M. Grätzel, *Adv. Energy Mater.* **2014**, *4*, 1400168.
[14] J. Lin, L. Zhao, Y.-U. Heo, L. Wang, F. H. Bijarbooneh, A. J. Mozer, A. Nattestad, Y. Yamauchi, S. X. Dou, J. H. Kim, *Nano Energy* **2015**, *11*, 557.
[15] T. T. T. Pham, T. Bessho, N. Mathews, S. M. Zakeeruddin, Y. M. Lam, S. Mhaisalkar, M. Grätzel, *J. Mater. Chem.* **2012**, *22*, 16201.
[16] N. Roy, Y. Sohn, D. Pradhan, *ACS Nano* **2013**, *7*, 2532.
[17] C. C. Dai Yunqian, Z. Jie, *Nano Lett.* **2009**, *9*, 2455.
[18] H. G. Yang, C. H. Sun, S. Z. Qiao, J. Zou, G. Liu, S. C. Smith, H. M. Cheng, G. Q. Lu, *Nature* **2008**, *453*, 638.
[19] X. Wu, Z. Chen, G. Q. M. Lu, L. Wang, *Adv. Funct Mater.* **2011**, *21*, 4167.
[20] a) T. Wei, C. Wan, Y. Wang, *Appl. Phys. Lett.* **2006**, *88*, 103122; b) T. C. Wei, C. C. Wan, Y. Y. Wang, C. M. Chen, H. S. Shiu, *J. Phys. Chem. C* **2007**, *111*, 4847; c) J. L. Lan, C. C. Wan, T. C. Wei, W. C. Hsu, Y. H. Chang, *Prog. Photovoltaics: Res. Appl.* **2012**, *20*, 44.
[21] Y. Chen, F. Huang, W. Xiang, D. Chen, L. Cao, L. Spiccia, R. A. Caruso, Y. B. Cheng, *Nanoscale* **2014**, *6*, 13787.
[22] a) J. Bisquert, D. Cahen, G. Hodes, S. Rühle, A. Zaban, *J. Phys. Chem. B* **2004**, *108*, 8106; b) F. Fabregat-Santiago, G. Garcia-Belmonte, I. Mora-Seró, J. Bisquert, *Phys. Chem. Chem. Phys.* **2011**, *13*, 9083.
[23] a) C. Z. Wen, H. B. Jiang, S. Z. Qiao, H. G. Yang, G. Q. M. Lu, *J. Mater. Chem.* **2011**, *21*, 7052; b) R. Gottesman, S. Tirosh, H.-N. Barad, A. Zaban, *J. Phys. Chem. Lett.* **2013**, *4*, 2822.
[24] B. Laskova, T. Moehl, L. Kavan, M. Zukalova, X. Liu, A. Yella, P. Comte, A. Zukal, M. K. Nazeeruddin, M. Graetzel, *Electrochim. Acta* **2015**, *160*, 296.
[25] S. Ito, T. N. Murakami, P. Comte, P. Liska, C. Grätzel, M. K. Nazeeruddin, M. Grätzel, *Thin Solid Films* **2008**, *516*, 4613.
[26] H. N. Tsao, P. Comte, C. Yi, M. Grätzel, *ChemPhysChem* **2012**, *13*, 2976.